Acta Mech 232, 1005–1023 (2021)
https://doi.org/10.1007/s00707-020-02899-x

ORIGINAL PAPER

Tran Huu Quoc · Vu Van Tham · Tran Minh Tu

Active vibration control of a piezoelectric functionally graded carbon nanotube-reinforced spherical shell panel

Received: 27 May 2020 / Revised: 21 October 2020 / Accepted: 26 November 2020 / Published online: 5 January 2021

Abstract A finite-element model is presented based on the four-variable shear deformation refined theory for active vibration control of a functionally graded carbon nanotube-reinforced composite spherical panel with integrated piezoelectric layers, acting as an actuator and a sensor. The linear distribution of the electric potential across the thickness of the piezoelectric layer and different distribution types of carbon nanotubes through the thickness of the layers are considered. The weak form of the governing equation is derived using Hamilton's principle, and a four-node nonconforming rectangular element with eight mechanical and two electrical degrees of freedom per node is introduced for discretising the domain. A constant velocity feedback approach is utilised for the active control of the panel by closed-loop control with a piezoelectric sensor and actuator. The convergence and accuracy of the model are validated by comparing numerical results with data available in literature. Some new parametric studies are also discussed in detail.

1 Introduction

Since they were invented by Iijima in 1991, carbon nanotubes (CNTs) have become a potential nanostructured material owing to their distinct mechanical and thermal properties and good electrical conductivity. Studies of their mechanical response have attracted the attention of many scientists [1–4]. Functionally graded carbon-nanotube-reinforced (CNTR) composite (FG-CNTRC) materials provide new advantages for composite materials. In FG-CNTRC, CNTs are designed to grade with specific rules along with desired directions within an isotropic matrix to enhance the mechanical properties of the structures. The addition of CNTs improves the mechanical, electrical, and thermal properties of the structures. In addition, the integration of laminated composites with piezoelectric materials provides structures with superior mechanical properties of composite materials and the capability to sense and adapt their static and dynamic responses. It can control the shape, size, vibration, and stability of these structures because of their direct and converse piezoelectric effects.

In the past few years, many analytical and numerical methods have been proposed for analysing the mechanical behaviours of FG-CNTRC structures. Using the element-free improved moving least-squares (IMLS)-Ritz method, Zhang et al. investigated the nonlinear bending response [5–8], vibration response [9–13], and dynamic response [14, 15] of FG-CNTRC plates and shells. Using the first-order shear deformation theory (FSDT) and *kp*-Ritz method, Lei et al. presented static, large deflection, and free vibration analysis of laminated FG-CNT plates [16, 17]. Based on a refined simplified two-variable *n*-th-higher-order plate theory, Bouazza and Zenkour [18] presented an exact closed-form formulation for free vibration analysis of composite plates reinforced with single-walled CNTs. The mechanical analysis of bulk CNTR nanocomposites and FG-CNTRC structures can be found in a review by Liew et al. [19].

T. H. Quoc (✉) · V. Van Tham · T. M. Tu
National University of Civil Engineering, Hai Ba Trung District, 55 Giai Phong Road, Hanoi 100000, Vietnam
e-mail: quocth@nuce.edu.vn

FG-CNTRC materials are often combined with smart materials, such as magnetostrictive materials, piezoelectric materials, electrostrictive materials, and shape memory alloys, to make intelligent structures.

The mechanical response of smart structures embedded with magnetostrictive layers has been discussed frequently [20–24]. Embedded piezoelectric actuators or sensors can be used to monitor the health of the structure and the structural integrity to adjust the shapes and focal points of space antennas and the contours of aircraft and spacecraft. In addition, the mechanical behaviours of FG-CNTRC structures integrated with piezoelectric patches or layers (PFG-CNTRC) have also been studied by several researchers. Using the three-dimensional theory of elasticity, Alibeigloo investigated the static vibration responses of PFG-CNTRC plates and cylindrical panels under mechanical uniform pressure, thermal load, and applied voltage field [25–29]. Rafiee et al. [30] analysed the nonlinear dynamic stability of PFG-CNTRC plates with initial geometric imperfections subjected to thermal and electrical loadings. Rafiee et al. [31] also investigated the large-amplitude free vibration of immovable simply supported PFG-CNTRC plates based on FSDT and von Kármán geometrical nonlinearity. Wu and Chang [32] investigated the 3D buckling problem of FG-CNTRC plates integrated with piezoelectric sensors and actuators. Mohsen Nasihatgozar et al. [33] investigated the effects of the volume fraction of CNTs, geometrical characteristics, and two axial and biaxial loading types on the buckling load of piezoelectric FG-CNTRC cylindrical panels based on the Donnell theory. Applying the Ritz energy approach, Ansari et al. [34] presented an analytical solution procedure for the nonlinear postbuckling analysis of PFG-CNTRC cylindrical shells subjected to combine electrothermal loading, axial compression, and lateral loads. Using Chebyshev polynomials in the Ritz method, Kiani [35] investigated the free vibration behaviour of FG-CNTRC plates with various mechanical and electrical boundary conditions. It was found that the natural frequency of a plate with a closed circuit is always lower than that of a plate with open-circuit boundary conditions. Kolahchi et al. [36] used the refined piezoelasticity zigzag theory and Hamilton's principle to discretise the governing equations for wave propagation in PFG-CNTRC plates. They found that the wave propagation of the system can be controlled effectively by the voltage applied to the actuator and the magnetic field exerted on the core. Setoodeh et al. [37] developed a model based on higher-order shear deformation theory and the differential quadrature method for the free vibration analysis of a PFG-CNTRC quadrilateral spherical panel. Using the formulation based on nonuniform rational B-spline basis functions, Nguyen-Quang et al. [38] proposed an extension of the isogeometric approach for the dynamic response of laminated PFG-CNTRC plates. Selim et al. [39] performed an impact analysis of PFG-CNTRC plates using the element-free IMLS-Ritz model with Reddy's higher-order shear deformation theory. By optimising the voltage distribution for the open-loop control and the displacement feedback control gain for the closed-loop control, Zhang et al. [40] presented an optimal shape control of FG-CNTRC plates with piezoelectric patches bonded at the top and bottom surfaces acting as actuators and sensors. Tran et al. [41, 42] developed a new four-variable shear deformation refined plate theory for the static and free vibration analysis of PFG-CNTRC plates.

There have been a limited number of studies regarding the active vibration control of FG-CNTRC structures with integrated piezoelectric actuators and sensors. Based on Reddy's higher-order shear deformation theory, Song et al. [43] presented the active vibration control of FG-CNTRC plates with surface-bonded piezoelectric actuators and sensors. Song et al. [44] also studied the active vibration control of an FG-CNTRC cylindrical shell with outer and inner surfaces with bonded piezoelectric patches acting as the actuator and sensor. Sharma et al. [45] implemented a finite-element model with a nonlinear fuzzy logic controller to perform active vibration control of FG-CNTRC plates. Zhang et al. [46] presented a solution based on Reddy's third-order shear deformation theory for active flutter control of CNTRC cylindrical panels in supersonic airflow. Selim et al. [47] presented a novel element-free IMLS-Ritz model based on Reddy's higher-order shear deformation theory for the active vibration control of FG-CNTRC plates with two positions of piezoelectric sensor and actuator layers.

Reviewing the literature reveals that various computational methods have been used to investigate the dynamic characteristics of FG-CNTRC structures integrated with a piezoelectric layer; however, there is no work available on the free vibration behaviour and active vibration control of PFG-CNTRC spherical shell panels. Therefore, in this study, a finite-element model based on the four-variable shear deformation refined theory for active vibration control of an FG-CNTRC spherical panel with an integrated actuator and sensor was developed. The extended rule of the mixture was used to estimate the material properties of the CNT-reinforced composite panel, and the electric potential was assumed to be a linear function through the thickness of each piezoelectric layer. The domain was discretised by a four-node nonconforming rectangular element with eight mechanical and two electrical degrees of freedom per node. A feedback control algorithm was used to achieve the mechanism of active control of the panel, and the Newmark method was employed to calculate the dynamic response of the hybrid spherical shell panels. The influence of material and geometry parameters, type of load,

and feedback control gains on the dynamic response of the hybrid spherical panel were also investigated and are discussed in detail.

2 Formulations

Figure 1 shows a smart piezoelectric spherical panel of a rectangular planform with constant principal radii of curvature R. The panel has three parts: the substrate, the piezoelectric layer at the top acting as an actuator, and the piezoelectric layer at the bottom acting as a sensor. The thickness of the substrate is h, and the thickness of each piezoelectric layer is h_p. The panel is discretised into a mesh of an $m \times n$ four-node flat shell element (rectangular elements) using the surface equation of the spherical panel $z = \frac{1}{2R}\left[\left(x - \frac{a}{2}\right)^2 + \left(y - \frac{a}{2}\right)^2\right]$.

2.1 Effective material properties of FG-CNTRC layer

In this research, the laminated substrate of the panel was made of perfectly bonded FG-CNT layers.

As shown in Fig. 2, five types of distribution of CNTs—UD, FG-O, FG-A, FG-V, and FG-X—are considered using the rule of mixture [48, 49]. Thus, the effective material properties of CNTRC can be written as [50]

$$E_{11}(z) = \eta_1 V_{\mathrm{CNT}}(z) E_{11}^{\mathrm{CNT}} + V_m(z) E^m, \tag{1}$$

$$\frac{\eta_2}{E_{22}(z)} = \frac{V_{\mathrm{CNT}}(z)}{E_{22}^{\mathrm{CNT}}} + \frac{V_m(z)}{E^m}, \tag{2}$$

$$\frac{\eta_3}{G_{12}(z)} = \frac{V_{\mathrm{CNT}}(z)}{G_{12}^{\mathrm{CNT}}} + \frac{V_m(z)}{G^m}, \tag{3}$$

$$\rho(z) = V_{\mathrm{CNT}}(z)\rho^{\mathrm{CNT}} + V_m(z)\rho^m, \tag{4}$$

$$\nu_{12} = V_{\mathrm{CNT}}^{*}\nu_{12}^{\mathrm{CNT}} + V_m(z)\nu^m. \tag{5}$$

where E_{11}^{CNT} and E_{22}^{CNT} are Young's moduli of the SWCNTs; G_{12}^{CNT} is the shear modulus of the same; E^m and G^m represent the corresponding properties of the isotropic matrix; η_1, η_2, and η_3 are the CNT/matrix

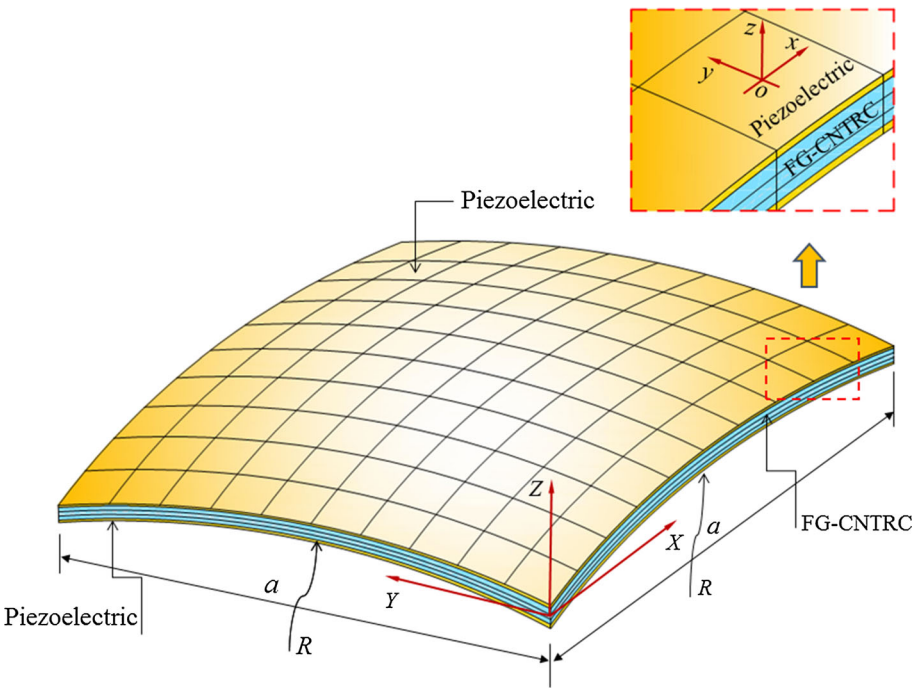

Fig. 1 Schematic of the smart piezoelectric FG-CNTRC spherical shell panel

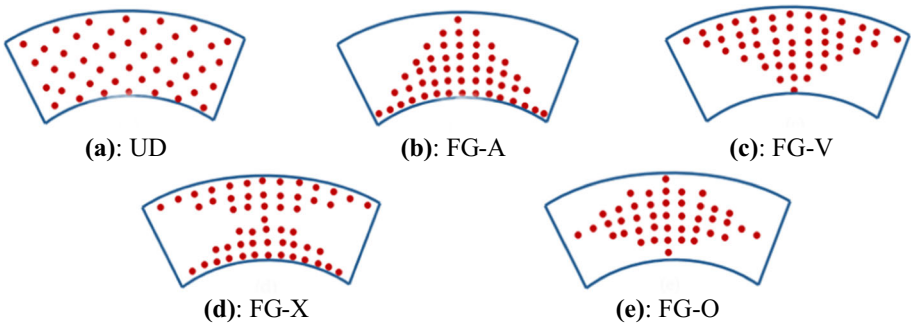

Fig. 2 Types of CNT distribution

efficiency parameters; ν_{12}^{CNT} and ν^m are the Poisson's ratios of CNT and matrix, respectively; $V_m(z)$ is the volume fraction of the matrix; and $V_{\mathrm{CNT}}(z)$ is the volume fraction of the CNT, which is assumed to be as follows [37]:

$$\text{UD: } \mathrm{V}_{\mathrm{CNT}}(z) = V_{\mathrm{CNT}}^{*}, \tag{6}$$

$$\text{FG-X: } V_{\mathrm{CNT}}(z) = 2V_{\mathrm{CNT}}^{*}\left(\frac{|2z - z_k - z_{k+1}|}{z_{k+1} - z_k}\right), \tag{7}$$

$$\text{FG-V: } V_{\mathrm{CNT}}(z) = 2V_{\mathrm{CNT}}^{*}\frac{z - z_k}{z_{k+1} - z_k}, \tag{8}$$

$$\text{FG-A: } V_{\mathrm{CNT}}(z) = 2V_{\mathrm{CNT}}^{*}\frac{z_{k+1} - z}{z_{k+1} - z_k}, \tag{9}$$

$$\text{FG-O: } V_{\mathrm{CNT}}(z) = 2V_{\mathrm{CNT}}^{*}\left(1 - \frac{|2z - z_k - z_{k+1}|}{z_{k+1} - z_k}\right). \tag{10}$$

Here, z_k and z_{k+1} are the coordinates of the k-th layer from the reference plane ($z = 0$), and V_{CNT}^{*} is the given volume fraction of the CNT,

$$V_{\mathrm{CNT}}^{*} = \frac{w_{\mathrm{CNT}}}{w_{\mathrm{CNT}} + \left(\rho^{\mathrm{CNT}}/\rho^{m}\right) - \left(\rho^{\mathrm{CNT}}/\rho^{m}\right)w_{\mathrm{CNT}}}, \tag{11}$$

where w_{CNT} is the mass fraction of the CNT, and ρ^{CNT} and ρ^{m} are the densities of the CNT and the matrix, respectively.

2.2 Approximation of the mechanical displacement

According to the four-variable shear deformation refined plate theory [42, 51], the displacement components u, v, and w of the flat shell element in the x-, y-, and z-directions of the local coordinate are expressed as

$$\begin{aligned} u(x, y, z, t) &= u_0(x, y, t) - z\frac{\partial w_b(x, y, t)}{\partial x} - f(z)\frac{\partial w_s(x, y, t)}{\partial x}; \\ v(x, y, z, t) &= v_0(x, y, t) - z\frac{\partial w_b(x, y, t)}{\partial y} - f(z)\frac{\partial w_s(x, y, t)}{\partial y}; \\ w(x, y, z, t) &= w_b(x, y, t) + w_s(x, y, t) \end{aligned} \tag{12}$$

where u_0 and v_0 are the in-plane displacements in the x- and y-directions, respectively, w_b and w_s are the bending and shear components of the transverse displacement, respectively, and $f(z) = z\left[-\frac{1}{8} + \frac{3}{2}\left(\frac{z}{h}\right)^2\right]$ [42] is the shape function of the distribution of the transverse shear strain and stress along with the structural thickness. Equation (12) can be written in matrix form as

$$\{d\} = [H]\left\{\overline{d}\right\} \tag{13}$$

where

$$\{d\} = \begin{Bmatrix} u & v & w \end{Bmatrix}^T, \tag{14}$$

$$[H] = \begin{bmatrix} 1 & 0 & 0 & -z & 0 & 0 & -f(z) & 0 \\ 0 & 1 & 0 & 0 & -z & 0 & 0 & -f(z) \\ 0 & 0 & 1 & 0 & 0 & 1 & 0 & 0 \end{bmatrix}, \tag{15}$$

$$\{\overline{d}\} = \begin{Bmatrix} u_0 & v_0 & w_b & w_{b,x} & w_{b,y} & w_s & w_{s,x} & w_{s,y} \end{Bmatrix}^T \tag{16}$$

where $\{\overline{d}\}$ is the nodal degree of freedom. In this study, a rectangular nonconforming bending element was used. The generalised displacements u_0 and v_0 are C^0 interpolated over an element as

$$\begin{aligned} u_0(x, y, t) &= \sum_{i=1}^{4} u_{oi}(t)\psi_i(\xi, \eta), \\ v_0(x, y, t) &= \sum_{i=1}^{4} v_{oi}(t)\psi_i(\xi, \eta) \end{aligned} \tag{17}$$

where ψ_i are linear interpolation functions:

$$\psi_i = \frac{1}{4}(1 + \xi\xi_i)(1 + \eta\eta_i), \quad (i = 1, 2, 3, 4). \tag{18}$$

Two components of the transverse displacement, w_b and w_s, are C^1 interpolated by the following expression:

$$\begin{aligned} w_b(x, y, t) &= \sum_{i=1}^{4} \left[w_b g_{i1}(\xi, \eta) + w_{b,x} g_{i2}(\xi, \eta) + w_{b,y} g_{i3}(\xi, \eta) \right], \\ w_s(x, y, t) &= \sum_{i=1}^{4} \left[w_s g_{i1}(\xi, \eta) + w_{s,x} g_{i2}(\xi, \eta) + w_{s,y} g_{i3}(\xi, \eta) \right] \end{aligned} \tag{19}$$

where g_{ij} $(j = 1, 2, 3)$ are nonconforming Hermite cubic interpolation functions:

$$\begin{aligned} g_{i1} &= \frac{1}{8}(1 + \xi_i\xi)(1 + \eta_i\eta)\left(2 + \xi_i\xi + \eta_i\eta - \xi^2 - \eta^2\right), \\ g_{i2} &= \frac{1}{8}\xi_i(\xi_i\xi - 1)(1 + \eta_i\eta)\left(1 + \xi_i^2\xi^2\right), \\ g_{i3} &= \frac{1}{8}\eta_i(1 + \xi_i\xi)(\eta_i\eta - 1)\left(1 + \eta_i^2\eta^2\right). \end{aligned} \tag{20}$$

By using Eqs. (17) and (19), Eq. (13) can be rewritten as

$$\{d\} = [H][N_m]\left\{d^e\right\} \tag{21}$$

where

$$[N_m] = \left[[N_{m1}] \; [N_{m2}] \; [N_{m3}] \; [N_{m4}] \right], \tag{22}$$

$$[N_{mi}] = \begin{bmatrix} \psi_i & 0 & 0 & 0 & 0 & 0 & 0 & 0 \\ 0 & \psi_i & 0 & 0 & 0 & 0 & 0 & 0 \\ 0 & 0 & g_{i1} & g_{i2} & g_{i3} & 0 & 0 & 0 \\ 0 & 0 & g_{i1,x} & g_{i2,x} & g_{i3,x} & 0 & 0 & 0 \\ 0 & 0 & g_{i1,y} & g_{i2,y} & g_{i3,y} & 0 & 0 & 0 \\ 0 & 0 & 0 & 0 & 0 & g_{i1} & g_{i2} & g_{i3} \\ 0 & 0 & 0 & 0 & 0 & g_{i1,x} & g_{i2,x} & g_{i3,x} \\ 0 & 0 & 0 & 0 & 0 & g_{i1,y} & g_{i2,y} & g_{i3,y} \end{bmatrix}. \tag{23}$$

The strains associated with the displacements are

$$\begin{Bmatrix} \varepsilon_x \\ \varepsilon_y \\ \gamma_{xy} \end{Bmatrix} = \begin{Bmatrix} u_{0,x} \\ v_{0,y} \\ u_{0,y} + v_{0,x} \end{Bmatrix} - z \begin{Bmatrix} w_{b,xx} \\ w_{b,yy} \\ w_{b,xy} \end{Bmatrix} - f(z) \begin{Bmatrix} w_{s,xx} \\ w_{s,yy} \\ w_{s,xy} \end{Bmatrix},$$
$$\begin{Bmatrix} \gamma_{yz} \\ \gamma_{xz} \end{Bmatrix} = g(z) \begin{Bmatrix} w_{s,x} \\ w_{s,y} \end{Bmatrix} \tag{24}$$

or in vector form

$$\{\varepsilon\} = \{\varepsilon^0\} - z\{\varepsilon^b\} - f(z)\{\varepsilon^s\},$$
$$\{\gamma\} = g(z)\{\gamma^s\}. \tag{25}$$

Substituting Eq. (21) into Eq. (25) yields

$$\{\varepsilon\} = \left[B_m^b\right]\{d^e\},$$
$$\{\gamma\} = \left[B_m^s\right]\{d^e\} \tag{26}$$

where

$$\left[B_m^b\right] = \left[\left[B_{m1}^b\right]\left[B_{m2}^b\right]\left[B_{m3}^b\right]\left[B_{m4}^b\right]\right] = \left[A_m^b\right] - z\left[C_m^b\right] - f(z)\left[D_m^b\right], \tag{27}$$
$$\left[B_m^s\right] = \left[\left[B_{m1}^s\right]\left[B_{m2}^s\right]\left[B_{m3}^s\right]\left[B_{m4}^s\right]\right] = g(z)\left[A_m^s\right] \tag{28}$$

in which

$$\left[A_{mi}^b\right] = \begin{bmatrix} \psi_{i,x} & 0 & 0 & 0 & 0 & 0 & 0 & 0 \\ 0 & \psi_{i,y} & 0 & 0 & 0 & 0 & 0 & 0 \\ \psi_{i,y} & \psi_{i,x} & 0 & 0 & 0 & 0 & 0 & 0 \end{bmatrix}, \tag{29}$$

$$\left[C_{mi}^b\right] = \begin{bmatrix} 0 & 0 & g_{i1,xx} & g_{i2,xx} & g_{i3,xx} & 0 & 0 & 0 \\ 0 & 0 & g_{i1,yy} & g_{i2,yy} & g_{i3,yy} & 0 & 0 & 0 \\ 0 & 0 & g_{i1,xy} & g_{i2,xy} & g_{i3,xy} & 0 & 0 & 0 \end{bmatrix}, \tag{30}$$

$$\left[D_{mi}^b\right] = \begin{bmatrix} 0 & 0 & 0 & 0 & 0 & g_{i1,xx} & g_{i2,xx} & g_{i3,xx} \\ 0 & 0 & 0 & 0 & 0 & g_{i1,yy} & g_{i2,yy} & g_{i3,yy} \\ 0 & 0 & 0 & 0 & 0 & g_{i1,xy} & g_{i3,xy} & g_{i3,xy} \end{bmatrix}, \tag{31}$$

$$\left[A_{mi}^s\right] = \begin{bmatrix} 0 & 0 & 0 & 0 & 0 & g_{i1,y} & g_{i2,y} & g_{i3,y} \\ 0 & 0 & 0 & 0 & 0 & g_{i1,x} & g_{i2,x} & g_{i3,x} \end{bmatrix}. \tag{32}$$

2.3 Approximation of the electric potentials

In this study, the approximation of the electric potential field of each piezoelectric layer is considered as a linear function through the thickness coordinate. Therefore, for the top and bottom surfaces of the panel, the electric potential functions are [52–54]

$$\Phi^t(x, y, z, t) = \frac{2z - h}{2h_p}\phi^t(x, y, t) = Z_p^t\phi^t(x, y, t) \quad \frac{h}{2} \le z \le \frac{h}{2} + h_p, \tag{33}$$
$$\Phi^b(x, y, z, t) = -\frac{2z + h}{2h_p}\phi^b(x, y, t) = Z_p^b\phi^b(x, y, t) \quad -\frac{h}{2} - h_p \le z \le -\frac{h}{2}. \tag{34}$$

It can be written in matrix form as

$$\{\Phi\} = \left[Z_p\right]\{\phi\} \tag{35}$$

where

$$\{\Phi\} = \left\{\Phi^t \ \Phi^b\right\}^T, \quad \left[Z_p\right] = \begin{bmatrix} Z_p^t & 0 \\ 0 & Z_p^b \end{bmatrix}, \quad \{\phi\} = \left\{\phi^t \ \phi^b\right\}^T. \tag{36}$$

The electric potential is also interpolated by C^0 interpolation:

$$\{\Phi\} = [Z_p][N_\phi]\{\phi^e\}. \tag{37}$$

The electric field E is derived from the electric potential:

$$\{E_i\} = \{\Phi_{,i}\} \quad (i = x, y, z). \tag{38}$$

Using Eqs. (34), (35), and (37), Eq. (38) can be rewritten as

$$\{E\} = [B_\phi]\{\phi^e\} \tag{39}$$

where

$$\{E\} = \{ E_x^t \; E_y^t \; E_z^t \; E_x^b \; E_y^b \; E_z^b \}^T, \tag{40}$$

$$[B_\phi] = [B_{\phi 1} \; B_{\phi 2} \; B_{\phi 3} \; B_{\phi 4}] \tag{41}$$

where

$$[B_{\phi i}] = \begin{bmatrix} Z_{p,x}^t & Z_{p,y}^t & Z_{p,z}^t & 0 & 0 & 0 \\ 0 & 0 & 0 & Z_{p,x}^b & Z_{p,y}^b & Z_{p,z}^b \end{bmatrix}^T. \tag{42}$$

2.4 Constitutive equations

The linear constitutive relations for a single FG-CNTRC layer can be written as

$$\begin{Bmatrix} \sigma_x^k \\ \sigma_y^k \\ \tau_{xy}^k \\ \tau_{yz}^k \\ \tau_{xz}^k \end{Bmatrix} = \begin{bmatrix} \overline{Q}_{11}^k(z) & \overline{Q}_{12}^k(z) & \overline{Q}_{16}^k(z) & 0 & 0 \\ \overline{Q}_{12}^k(z) & \overline{Q}_{22}^k(z) & \overline{Q}_{26}^k(z) & 0 & 0 \\ \overline{Q}_{16}^k(z) & \overline{Q}_{26}^k(z) & \overline{Q}_{66}^k(z) & 0 & 0 \\ 0 & 0 & 0 & \overline{Q}_{44}^k(z) & \overline{Q}_{45}^k(z) \\ 0 & 0 & 0 & \overline{Q}_{45}^k(z) & \overline{Q}_{55}^k(z) \end{bmatrix} \begin{Bmatrix} \varepsilon_x \\ \varepsilon_y \\ \gamma_{xy} \\ \gamma_{yz} \\ \gamma_{xz} \end{Bmatrix} \tag{43}$$

where $\overline{Q}_{ij}$ are the transformed material constants expressed in terms of material constants [55]:

$$\begin{aligned}
\overline{Q}_{11}^k(z) &= Q_{11}^C(z)\cos^4\theta^k + 2\Big[Q_{12}^C(z) + 2Q_{66}^C(z)\Big]\sin^2\theta^k\cos^2\theta^k + Q_{22}^C(z)\sin^4\theta^k, \\
\overline{Q}_{12}^k(z) &= \Big[Q_{11}^C(z) + Q_{22}^C(z) - 4Q_{66}^C(z)\Big]\sin^2\theta^k\cos^2\theta^k + Q_{12}^C(z)\Big(\sin^4\theta^k + \cos^4\theta^k\Big), \\
\overline{Q}_{22}^k(z) &= Q_{11}^C(z)\sin^4\theta^k + 2\Big[Q_{12}^C(z) + 2Q_{66}^C(z)\Big]\sin^2\theta^k\cos^2\theta^k + Q_{22}^C(z)\cos^4\theta^k, \\
\overline{Q}_{16}^k(z) &= \Big[Q_{11}^C(z) - Q_{12}^C(z) - 2Q_{66}^C(z)\Big]\sin\theta^k\cos^3\theta^k \\
&\quad + \Big[Q_{12}^C(z) - Q_{22}^C(z) + 2Q_{66}^C(z)\Big]\sin^3\theta^k\cos\theta^k, \\
\overline{Q}_{26}^k(z) &= \Big[Q_{11}^C(z) - Q_{12}^C(z) - 2Q_{66}^C(z)\Big]\sin^3\theta^k\cos\theta^k \\
&\quad + \Big[Q_{12}^C(z) - Q_{22}^C(z) + 2Q_{66}^C(z)\Big]\sin\theta^k\cos^3\theta^k, \\
\overline{Q}_{66}^k(z) &= \Big[Q_{11}^C(z) + Q_{22}^C(z) - 2Q_{12}^C(z) - 2Q_{66}^C(z)\Big]\sin^2\theta^k\cos^2\theta^k \\
&\quad + Q_{66}^C(z)\Big(\sin^4\theta^k + \cos^4\theta^k\Big), \\
\overline{Q}_{44}^k(z) &= Q_{44}^C(z)\cos^2\theta^k + Q_{55}^C(z)\sin^2\theta^k, \\
\overline{Q}_{45}^k(z) &= \Big[Q_{55}^C(z) - Q_{44}^C(z)\Big]\cos\theta^k\sin\theta^k, \\
\overline{Q}_{55}^k(z) &= Q_{55}^C(z)\cos^2\theta^k + Q_{44}^C(z)\sin^2\theta^k
\end{aligned} \tag{44}$$

where $Q_{ij}^{C}(z)$ are the plane stress-reduced stiffness values, which are defined in terms of the engineering constants in the layer material axes. For each CNT layer,

$$Q_{11}^{C}(z)=\frac{E_{11}(z)}{1-\nu_{12}\nu_{21}};\quad Q_{12}^{C}(z)=\frac{\nu_{12}E_{22}(z)}{1-\nu_{12}\nu_{21}};\quad Q_{22}^{C}(z)=\frac{E_{22}(z)}{1-\nu_{12}\nu_{21}};$$
$$Q_{44}^{C}(z)=G_{23}^{C}(z);\quad Q_{55}^{C}(z)=G_{13}^{C}(z);\quad Q_{66}^{C}(z)=G_{12}^{C}(z). \tag{45}$$

The linear constitutive relations for an individual piezoelectric material layer can be expressed as [56–58]

$$\begin{Bmatrix}\sigma_x^k\\ \sigma_y^k\\ \tau_{xy}^k\\ \tau_{yz}^k\\ \tau_{xz}^k\end{Bmatrix}=\begin{bmatrix}\overline{C}_{11} & \overline{C}_{12} & 0 & 0 & 0\\ \overline{C}_{12} & \overline{C}_{11} & 0 & 0 & 0\\ 0 & 0 & \frac{1}{2}\left(\overline{C}_{11}-\overline{C}_{12}\right) & 0 & 0\\ 0 & 0 & 0 & \overline{C}_{55} & 0\\ 0 & 0 & 0 & 0 & \overline{C}_{55}\end{bmatrix}\begin{Bmatrix}\varepsilon_x\\ \varepsilon_y\\ \gamma_{xy}\\ \gamma_{yz}\\ \gamma_{xz}\end{Bmatrix}-\begin{bmatrix}0 & 0 & \overline{e}_{31}\\ 0 & 0 & \overline{e}_{31}\\ 0 & 0 & 0\\ 0 & -e_{15} & 0\\ -e_{15} & 0 & 0\end{bmatrix}\begin{Bmatrix}E_x^k\\ E_y^k\\ E_z^k\end{Bmatrix}, \tag{46}$$

$$\begin{Bmatrix}D_x^k\\ D_y^k\\ D_z^k\end{Bmatrix}=\begin{bmatrix}0 & 0 & 0\,0 & -e_{15}\\ 0 & 0 & 0\,-e_{15} & 0\\ \overline{e}_{31} & \overline{e}_{31} & 0\,0 & 0\end{bmatrix}\begin{Bmatrix}\varepsilon_x\\ \varepsilon_y\\ \gamma_{xy}\\ \gamma_{yz}\\ \gamma_{xz}\end{Bmatrix}+\begin{bmatrix}p_{11} & 0 & 0\\ 0 & p_{11} & 0\\ 0 & 0 & \overline{p}_{33}\end{bmatrix}\begin{Bmatrix}E_x^k\\ E_y^k\\ E_z^k\end{Bmatrix}. \tag{47}$$

The elastic constants for the piezoelectric layer are

$$\overline{C}_{11}=C_{11}-\frac{(C_{13})^2}{C_{33}};\quad \overline{C}_{12}=C_{12}-\frac{(C_{13})^2}{C_{33}};\quad \overline{C}_{55}=C_{55};$$
$$\overline{e}_{31}=e_{31}-\frac{C_{13}}{C_{33}}e_{33};\quad \overline{p}_{33}=p_{33}+\frac{e_{33}^2}{C_{33}} \tag{48}$$

where $[C_{\mathrm{ij}}]$ is the elastic constant matrix of the piezoelectric layers, $[e_{\mathrm{ij}}]$ is the electromechanical coupling matrix, $[p_{\mathrm{ij}}]$ is the dielectric permittivity matrix, $\{E\}$ is the electric field, and $\{D\}$ is the electrical displacement in the piezoelectric layer. The coupling between the elastic and electric fields can be rewritten in short form as

$$\{\sigma\}=[Q]\{\varepsilon\}-[e]\{E\},$$
$$\{D\}=[e]^T\{\varepsilon\}+[p]\{E\}. \tag{49}$$

2.5 Governing equations of motion

The dynamic equations of the hybrid panel can be derived using Hamilton's variational principle,

$$\delta\int_{t_1}^{t_2}[T-U+W]dt=0, \tag{50}$$

where T, U, and W are the kinetic energy, strain energy, and work done by the applied forces, respectively.

At the element level, the kinetic energy can be calculated as

$$T^e=\frac{1}{2}\int_{V_e}\rho\{\dot{d}\}^T\{\dot{d}\}\mathrm{d}V_e. \tag{51}$$

The strain energy can be written as

$$U^e=\frac{1}{2}\int_{V_e}\left[\{\varepsilon\}^T\{\sigma\}+\{\gamma\}^T\{\tau\}-\{E\}^T\{D\}\right]dV_e, \tag{52}$$

and the work done by the external forces is

$$W^e=\int_{V_e}\{d\}^T\{f_b\}dV_e+\int_{A_e}\{d\}^T\{f_s\}\mathrm{d}A_e+\{d\}^T\{f_c\} \tag{53}$$

where V_e is the volume of the element, $\{f_b\}$ is the body force, A_e is the surface area of the element where the surface force $\{f_s\}$ is specified, and $\{f_c\}$ is the concentrated load.

The elementary governing equation of motion can be derived by substituting Eqs. (21), (26), (39), and (49) into Eqs. (51), (52), (53), and Eq. (50),

$$\begin{bmatrix} M_{mm} & 0 \\ 0 & 0 \end{bmatrix}_e \begin{Bmatrix} \ddot{d} \\ \ddot{\phi} \end{Bmatrix}_e + \begin{bmatrix} K_{mm} & K_{m\phi} \\ K_{\phi m} & K_{\phi\phi} \end{bmatrix}_e \begin{Bmatrix} d \\ \phi \end{Bmatrix}_e = \begin{Bmatrix} F_m \\ F_\phi \end{Bmatrix}_e, \tag{54}$$

where

$$\begin{aligned}
[M_{mm}]_e &= \int_{A_e} [N_m]^T [m][N_m] dA_e, \\
[K_{mm}]_e &= \left[K^b_{mm}\right]_e + \left[K^s_{mm}\right]_e = \int_{A_e} \left[B^b_m\right]^T \left[\overline{D}_b\right] \left[B^b_m\right] dA_e + \int_{A_e} \left[B^s_m\right]^T \left[\overline{D}_s\right] \left[B^s_m\right] dA_e, \\
\left[K_{m\phi}\right]_e &= \left[K_{\phi m}\right]^T_e = \int_{A_e} [B_m]^T [e][B_m] dA_e, \\
\left[K_{\phi\phi}\right]_e; &= \int_{A_e} \left[B_\phi\right]^T [p] \left[B_\phi\right] dA_e.
\end{aligned} \tag{55}$$

Withdrawing ϕ from the second equation and then substituting it into the first equation in Eq. (54), one obtains the final form of the governing equation in shortened form:

$$[M_{mm}]_e \left\{\ddot{d}\right\}_e + \left([K_{mm}]_e + \left[K_{m\phi}\right]_e \left[K_{\phi\phi}\right]^{-1}_e \left[K_{\phi m}\right]_e\right)\{d\}_e = \{F_m\}_e + \left[K_{m\phi}\right]_e \left[K_{\phi\phi}\right]^{-1}_e \left\{F_\phi\right\}_e. \tag{56}$$

The global equations of motion can be obtained by assembling the element equations and are given by

$$[M_{mm}]\left\{\ddot{d}\right\} + \left([K_{mm}] + \left[K_{m\phi}\right]\left[K_{\phi\phi}\right]^{-1}\left[K_{\phi m}\right]\right)\{d\} = \{F_m\} + \left[K_{m\phi}\right]\left[K_{\phi\phi}\right]^{-1}\left\{F_\phi\right\} \tag{57}$$

where

$$\begin{aligned}
[M_{mm}] &= \sum_{i=1}^{m\times n} [\Lambda]^T_i [M_{mm}]_{ei} [\Lambda]_i, \quad [K_{mm}] = \sum_{i=1}^{m\times n} [\Lambda]^T_i [K_{mm}]_{ei} [\Lambda]_i, \quad [F_m] = \sum_{i=1}^{m\times n} [\Lambda]^T_i [F_m]_{ei}, \\
\left[K_{m\phi}\right] &= \sum_{i=1}^{m\times n} [\Lambda]^T_i \left[K_{m\phi}\right]_{ei} [\Lambda]_i, \quad \left[K_{\phi\phi}\right] = \sum_{i=1}^{m\times n} [\Lambda]^T_i \left[K_{\phi\phi}\right]_{ei} [\Lambda]_i, \quad \left[F_\phi\right] = \sum_{i=1}^{m\times n} [\Lambda]^T_i \left[F_\phi\right]_{ei}, \\
\left[K_{\phi m}\right] &= \sum_{i=1}^{m\times n} [\Lambda]^T_i \left[K_{\phi m}\right]_{ei} [\Lambda]_i.
\end{aligned}$$

Here, $[\Lambda]$ is the global–local transformation matrix.

2.6 Active control analysis

In this study, the piezoelectric actuator and sensor were bonded at the top and bottom surfaces, respectively. The actuator and sensor are denoted by subscripts a and s, respectively. Without an external charge, the generated potential on the sensor can be obtained from Eq. (54):

$$\phi_s = \left[K^{-1}_{\phi\phi}\right]_s \left[K_{\phi m}\right]_s d_s. \tag{58}$$

By using closed-loop feedback control, the voltage on the actuator can be written as

$$\phi_a = G_d \phi_s + G_v \dot{\phi}_s \tag{59}$$

where G_d and G_v are the displacement and feedback control gains, respectively. This implies that, when the panel is in the vibration state, electric charges are generated in the sensor layer and then amplified and converted into the signal. The signal is then fed back into the distributed actuator, and an input voltage for the actuator

is generated. Owing to the piezoelectric effect, stresses and strains are generated. Substituting Eqs. (58), (59) into Eq. (54) gives

$$F_a = \left[K_{\phi m}\right]_a d_a - G_d\left[K_{\phi\phi}\right]_a\left[K_{\phi\phi}^{-1}\right]_s\left[K_{\phi m}\right]_s d_s - G_v\left[K_{\phi\phi}\right]_a\left[K_{\phi\phi}^{-1}\right]_s\left[K_{\phi m}\right]_s \dot{d}_s. \tag{60}$$

Substituting Eq. (59) into Eq. (56), one writes

$$[M_{mm}]\{\ddot{d}\} + [C_a]\{\dot{d}\} + \left[K^*\right]\{d\} = \{F\} \tag{61}$$

where

$$\left[K^*\right] = [K_{mm}] + G_d\left[K_{m\phi}\right]_s\left[K_{\phi\phi}^{-1}\right]_s\left[K_{\phi m}\right], \tag{62}$$

$$[C_a] = G_v\left[K_{m\phi}\right]_s\left[K_{\phi\phi}^{-1}\right]_s\left[K_{\phi m}\right]_s. \tag{63}$$

Considering the structure damping effect, Eq. (60) can be rewritten as

$$[M_{mm}]\{\ddot{d}\} + ([C_a] + [C_R])\{\dot{d}\} + \left[K^*\right]\{d\} = \{F\} \tag{64}$$

with

$$[C_R] = \alpha_R[M_{mm}] + \beta_R[K_{mm}] \tag{65}$$

where α_R and β_R are Rayleigh damping coefficients that can be determined from experiments.

3 Numerical results

Comparison studies were performed to prove the convergence and accuracy of the finite-element model. Furthermore, parametric studies were performed to study the effects of the CNT volume fraction, type of CNT distribution, thickness of the piezoelectric layer, laminate configurations, and mechanical and electrical boundary conditions on the natural frequencies of the panel. Finally, active vibration control results were obtained to illustrate the effectiveness of the type of load and feedback control gains on the dynamic behaviour of the PFG-CNTRC spherical shell panels. The following material properties are used in various examples.

- *Material 1* (Al_2O_3) [59]:
  $E = 380$ GPa, $\nu = 0.3$, $\rho = 3800$ kg/m^3.
- *Material 2* (PZT-4) [59]:
  $C_{11} = 139$ GPa, $C_{12} = 77.8$ GPa, $C_{13} = 74.3$ GPa, $C_{33} = 115$ GPa, $C_{44} = C_{55} = 25.6$ GPa, $C_{66} = 30.6$ GPa, $\rho = 7500$ kg/m^3, $e_{31} = -5.2$ C/m^2, $e_{33} = 15.1$ C/m^2, $e_{15} = 12.7$ C/m^2, $p_{11} = 6.75$ nF/m, $p_{33} = 5.9$ nF/m.
- *Material 3* (PZT-5A) [38]:
  $E = 63$ GPa, $G = 23.3$ GPa, $\nu = 0.35$, $\rho = 7750$ kg/m^3, $e_{31} = e_{32} = -7.209$ C/m^2, $e_{33} = 15.12$ C/m^2, $e_{15} = e_{24} = 12.322$ C/m^2, $p_{11} = p_{22} = 1.53 \times 10^{-8}$ F/m, $p_{33} = 1.5 \times 10^{-8}$ F/m.
- *Material 4* [38]:
  Material 4 in this study is FG-CNTRC with the properties of the matrix and reinforcement as follows:

The matrix (PMMA): $E^m = (3.52 - 0.0034\,\Delta T)$ GPa, $\nu^m = 0.34$, and $\rho^m = 1150$ kg/m^3. Here, $\Delta T = T - T_0$ is the temperature change, and T_0 is the reference temperature, which is set to 300 K.

The reinforcement (armchair SWCNT): ${E_{11}}^{\mathrm{CNT}} = 5.64$ TPa, ${E_{22}}^{\mathrm{CNT}} = 7.0800$ TPa, ${G_{12}}^{\mathrm{CNT}} = 1.9455$ TPa, ${\nu_{12}}^{\mathrm{CNT}} = 0.175$, and ${\rho}^{\mathrm{CNT}} = 1400$ kg/m^3. For three different volume fractions of CNTs, the efficiency parameters are $\eta_1 = 0.137$ and $\eta_2 = 1.022$ for $V^*_{\mathrm{CNT}} = 0.12$, $\eta_1 = 0.142$ and $\eta_2 = 1.626$ for $V^*_{\mathrm{CNT}} = 0.17$, and $\eta_1 = 0.141$ and $\eta_2 = 1.585$ for $V^*_{\mathrm{CNT}} = 0.28$. For each case, the efficiency parameter η_3 is $0.7\eta_2$.

Table 1 Fundamental natural frequency of the doubly curved isotropic shell coupled with piezoelectric layers ($a/b = 1$, $h/a = 0.1$, and $R_y/a = 5$)

a/R_x	h_p/h	$f_{Clc}(Hz)$			$f_{Opc}(Hz)$		
		Present	Ref. [59]	Diff. (%)	Present	Ref. [59]	Diff. (%)
− 0.2	0.1	826.399	824.049	0.29	844.145	841.189	0.35
	0.2	795.966	788.430	0.96	828.307	820.477	0.95
0	0.1	835.201	839.368	− 0.50	852.815	856.455	− 0.43
	0.2	803.351	801.794	0.19	835.427	833.781	0.20
0.1	0.1	846.659	853.147	− 0.76	864.135	870.057	− 0.68
	0.2	813.070	813.413	− 0.04	844.859	845.108	− 0.03
0.2	0.1	862.425	870.705	− 0.95	879.730	887.350	− 0.86
	0.2	826.504	828.101	− 0.19	857.925	859.347	− 0.17

3.1 Convergence and comparison studies

The first example considered is the simply supported (SSSS) double-curved shell panel made of material 1 with integrated piezoelectric layers PZT4 at the top and bottom surfaces. Table 1 summarises a comparison of the fundamental natural frequencies in open-circuit (Opc) and closed-circuit (Clc) electrical conditions of the panel. It can be seen that, with a meshing of 20×20 elements, the results obtained by the present model are in good agreement with those obtained by Sayyadi [59] based on higher-order deformation theory. The difference between the present results and the results of Sayyadi [59] is less than 1% for various inlet parameters, such as a/R_x ratio, h_p/h ratio, and closed and open electrical boundary conditions.

The second example was considered for the PFG-CNTRC square plates. The results obtained were compared with those given by Nguyen-Quang et al. [38] based on an isogeometric approach and higher-order deformation theory. The dimensions of the plates were set to $a = b = 0.4$ m, $h = a/20$, and $h_p = h/10$; the substrate was made of material 4; and the piezoelectric layers were made of material 3. Table 2 lists the first natural frequencies of the single-layer plates, while Table 3 lists those of the multilayer plates. A meshing of 20×20 elements was chosen to achieve extremely good agreement between the present results and the results reported elsewhere [38] for various mechanical and electrical boundary conditions, various CNT volume fractions, and different types of CNT distribution. Consequently, the meshing of 20×20 elements was used for all further analyses in this work.

3.2 Free vibration analysis of PFG-CNTRC spherical shell panels

This example considers an FG-CNTRC spherical shell panel made of material 4. The panel has a square plane projection with $a = 0.4$ m, thickness $h = 0.02$ m, and radius $R = 2$ m. Two piezoelectric layers of PZT-5A with $h_p = 0.002$ m are bonded on the top and bottom surfaces of the panel. Tables 4 and 5 list the first natural frequencies of the PFG-CNTRC spherical shell panel for different parameters of material properties and different mechanical and electrical boundary conditions. The results illustrate that, with the increase in the CNT volume fraction, the frequency of the panel increases accordingly. The laminate configuration with $[-45/45]_{as}$ is more effective than any other configuration. Among the four types of CNT distributions, the FG-X type has the highest frequency, whereas the FG-O type has the lowest frequency for the same other input parameters. The results show that the natural frequencies of the hybrid panel in the case of CCCC are higher than those of the other considered boundary conditions. It can also be seen that the natural frequencies of the hybrid panel are higher in the open-circuit case than in the closed-circuit case because the open circuit converts the electric potential to mechanical energy during vibration, while the closed circuit does not.

3.3 Dynamic vibration control of PFG-CNTRC spherical shell panels

A fully clamped (CCCC) PFG-CNTRC spherical panel, with lamination sequence [**a**/0/90/0/**s**], where **a** and **s** represent the piezoelectric actuator and sensor layers made of PZT-5A, bonded on the upper and lower surfaces, respectively, is considered. The substrate is made of material 4. The side dimension is $a = 0.4$ m, the thickness

Table 2 Fundamental natural frequency f (in Hz) of the single-layer PPG-CNTRC square plates ($a = b$, $a/h = 20$, [$p/0/p$], and $h_p/h = 1/10$)

V^*_{CNT}	Type	Condition	Boundary conditions					
			SSSS			CFFF		
			Present	Ref. [38]	Diff. (%)	Present	Ref. [38]	Diff. (%)
0.12	UD	Clc	586.221	582.992	0.55	145.631	145.473	0.05
		Opc	620.640	627.204	− 1.05	149.590	150.359	0.51
	FG-X	Clc	625.575	621.782	0.61	166.290	166.487	− 0.21
		Opc	657.436	662.752	− 0.80	169.750	170.738	0.15
	FG-V	Clc	563.095	559.827	0.58	132.273	131.928	0.31
		Opc	599.299	606.301	− 1.15	136.850	137.588	0.96
	FG-O	Clc	543.439	540.374	0.57	121.019	120.947	0.52
		Opc	580.981	588.575	− 1.29	125.759	126.378	1.12
0.17	UD	Clc	626.699	622.893	0.61	165.097	165.065	− 0.10
		Opc	658.679	654.465	0.64	168.598	169.365	0.27
	FG-X	Clc	679.830	675.135	0.70	191.150	191.621	− 0.37
		Opc	708.791	703.692	0.72	194.154	195.287	− 0.08
	FG-V	Clc	593.762	589.734	0.68	147.046	146.738	0.18
		Opc	628.024	623.499	0.73	151.206	151.863	0.74
	FG-O	Clc	567.649	563.816	0.68	133.215	132.676	0.39
		Opc	603.530	599.371	0.69	137.546	138.037	0.91
0.28	UD	Clc	690.332	685.587	0.69	196.726	197.147	− 0.21
		Opc	718.529	721.919	− 0.47	199.614	200.669	− 0.53
	FG-X	Clc	765.505	757.950	1.00	230.638	231.928	− 0.56
		Opc	790.164	789.814	0.04	233.060	234.852	− 0.76
	FG-V	Clc	640.715	637.353	0.53	171.531	171.477	0.03
		Opc	671.888	677.399	− 0.81	175.081	175.830	− 0.43
	FG-O	Clc	603.764	601.032	0.45	153.783	153.361	0.28
		Opc	636.960	643.745	− 1.05	157.513	157.965	− 0.29

Table 3 Fundamental natural frequency f (in Hz) of the multilayer PFG-CNTRC square plates ($a = b$, $a/h = 20$, and $h_p/h = 1/10$)

V^*_{CNT}	Type	Condition	Laminate configurations					
			[p/0/90/0/p]			[p/− 45/45/− 45/45/p]		
			Present	Ref. [38]	Diff. (%)	Present	Ref. [38]	Diff. (%)
0.12	UD	Clc	587.129	583.510	0.62	653.778	650.401	0.52
		Opc	621.628	627.716	− 0.97	684.420	689.664	− 0.76
	FG-X	Clc	593.339	588.372	0.84	660.824	655.204	0.86
		Opc	627.438	632.184	− 0.75	691.089	694.142	− 0.44
	FG-V	Clc	585.376	581.714	0.63	651.538	648.169	0.52
		Opc	620.096	626.205	− 0.98	682.397	687.708	− 0.77
	FG-O	Clc	581.003	578.737	0.39	646.759	645.708	0.16
		Opc	615.910	623.343	− 1.19	677.790	685.299	− 1.10
0.17	UD	Clc	627.696	624.543	0.50	714.696	712.200	0.35
		Opc	659.749	665.615	− 0.88	742.383	747.626	− 0.70
	FG-X	Clc	636.287	631.317	0.79	724.125	718.700	0.75
		Opc	667.860	671.913	− 0.60	751.393	753.763	− 0.31
	FG-V	Clc	625.134	621.914	0.52	711.629	709.145	0.35
		Opc	657.473	663.359	− 0.89	739.570	744.893	− 0.71
	FG-O	Clc	619.417	618.126	0.21	705.529	706.112	− 0.08
		Opc	651.961	659.687	− 1.17	733.654	741.912	− 1.11
0.28	UD	Clc	691.467	686.852	0.67	808.612	808.572	0.00
		Opc	719.724	723.150	− 0.47	832.038	838.388	− 0.76
	FG-X	Clc	704.344	697.260	1.02	822.251	818.211	0.49
		Opc	732.039	732.991	− 0.13	845.236	847.654	− 0.29
	FG-V	Clc	687.605	682.974	0.68	804.663	804.564	0.01
		Opc	716.255	719.788	− 0.49	828.399	834.775	− 0.76
	FG-O	Clc	679.772	677.986	0.26	796.483	800.689	− 0.53
		Opc	708.637	714.904	− 0.88	820.405	830.949	− 1.27

Table 4 Fundamental natural frequency f (in Hz) of the laminated PFG-CNTRC spherical shell panels ($a/h = 20$ and $R/a = 5$)

V^*_{CNT}	Type	Electrical condition	Laminate configurations					
			[p/0/90/0/p]		[p/− 30/30/− 30/30/p]		[p/− 45/45/− 45/45/p]	
			$a/h = 20$	$a/h = 50$	$a/h = 20$	$a/h = 50$	$a/h = 20$	$a/h = 50$
0.12	UD	Clc	618.915	315.473	701.280	409.270	739.058	455.872
		Opc	651.678	327.422	732.549	424.551	767.861	468.565
	FG-X	Clc	624.847	317.643	707.537	412.198	746.210	459.723
		Opc	657.25	329.496	738.501	427.422	774.675	472.313
	FG-V	Clc	622.494	319.475	696.697	406.597	735.556	454.135
		Opc	654.775	330.999	727.394	421.305	763.740	466.249
	FG-O	Clc	613.115	313.428	695.136	406.457	731.964	452.059
		Opc	646.241	325.472	726.708	421.778	761.111	464.851
0.17	UD	Clc	660.769	336.039	765.171	452.741	816.825	517.892
		Opc	691.149	347.039	793.868	467.440	842.447	529.203
	FG-X	Clc	669.031	339.145	773.542	456.577	826.247	522.872
		Opc	698.984	350.034	801.892	471.199	851.506	534.071
	FG-V	Clc	664.258	340.474	759.659	449.728	812.924	516.170
		Opc	694.246	351.087	787.741	463.801	837.943	526.916
	FG-O	Clc	652.985	333.373	757.339	449.394	807.797	513.128
		Opc	683.799	344.476	786.376	464.128	833.797	524.545
0.28	UD	Clc	722.484	361.120	855.694	508.424	932.770	612.617
		Opc	749.349	371.023	880.929	522.880	953.879	622.101
	FG-X	Clc	735.179	366.347	868.178	514.349	946.299	619.656
		Opc	761.534	376.106	893.009	528.658	967.051	629.025
	FG-V	Clc	724.989	365.801	849.879	505.737	929.143	611.281
		Opc	751.675	375.406	874.447	519.455	949.745	620.261
	FG-O	Clc	711.645	357.609	845.870	504.821	921.457	606.629
		Opc	739.044	367.627	871.492	519.288	942.990	616.235

Table 5 Fundamental natural frequency f (in Hz) of the laminated PFG-CNTRC spherical shell panels ($a = b$, $a/h = 20$, and $R/a = 5$)

V^*_{CNT}	Type	Electrical condition	Boundary conditions					
			[p/0/90/0/90/0/p]					
			CCCC	CCCF	CFCF	CFFF	SCSC	SSSS
0.12	UD	Clc	1134.877	869.749	827.754	139.848	868.470	619.027
		Opc	1181.638	891.970	848.495	143.972	913.823	651.762
	FG-X	Clc	1142.206	876.706	834.562	141.174	873.379	622.246
		Opc	1188.461	898.673	855.039	145.264	918.378	654.783
	FG-V	Clc	1133.261	868.020	826.282	139.551	868.439	621.744
		Opc	1179.909	890.353	847.127	143.680	913.557	654.138
	FG-O	Clc	1127.806	862.872	821.020	138.518	863.794	615.980
		Opc	1175.090	885.355	842.036	142.675	909.503	648.912
0.17	UD	Clc	1230.811	961.829	916.561	157.103	929.051	660.862
		Opc	1272.230	981.198	934.368	160.790	970.803	691.222
	FG-X	Clc	1240.736	970.869	925.337	158.823	935.953	665.421
		Opc	1281.616	989.981	942.883	162.475	977.292	695.545
	FG-V	Clc	1229.097	959.925	914.970	156.710	928.959	663.843
		Opc	1270.446	979.413	932.887	160.404	970.512	693.902
	FG-O	Clc	1221.924	953.359	908.370	155.401	922.953	656.853
		Opc	1263.935	973.011	926.471	159.122	965.130	687.444
0.28	UD	Clc	1362.621	1089.947	1036.569	184.709	1015.349	722.517
		Opc	1395.756	1105.161	1050.165	187.816	1051.385	749.370
	FG-X	Clc	1377.865	1103.131	1049.359	187.099	1026.326	729.832
		Opc	1410.524	1118.129	1062.744	190.174	1061.915	756.410
	FG-V	Clc	1362.458	1089.330	1036.418	184.219	1015.742	725.648
		Opc	1395.675	1104.703	1050.169	187.338	1051.705	752.316
	FG-O	Clc	1352.515	1080.474	1027.689	182.477	1007.674	717.201
		Opc	1386.352	1096.015	1041.618	185.621	1044.249	744.339

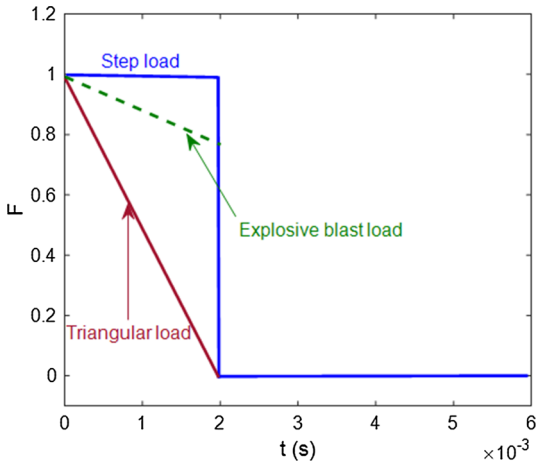

Fig. 3 Types of load: step load, triangular load, and explosive load

of the substrate $h = 0.04$ m, the thickness of each piezoelectric layer $h_p = 0.004$ m, and radius $R = 2$ m. The panel is subjected to sinusoidally distributed transverse loads expressed as

$$q = q_0 \sin\left(\frac{\pi x}{a}\right) \sin\left(\frac{\pi y}{b}\right) F(t) \tag{66}$$

where $F(t)$ is defined as

$$F(t) = \begin{bmatrix} \begin{cases} 1 & 0 \le t \le t_1 \text{ Step load} \\ 0 & t > t_1 \end{cases} \\ \begin{cases} 1 - t/t_1 & 0 \le t \le t_1 \text{ Triangular load} \\ 0 & t > t_1 \end{cases} \\ \begin{cases} e^{-\gamma t}\, e^{-\gamma t} & 0 \le t \le t_1 \text{ Explosive blast load} \\ 0 & t > t_1 \end{cases} \end{bmatrix} \tag{67}$$

in which $q_0 = 10^4$ N/m^2, $\gamma = 330$ s^{-1}, $t_1 = 0.002$ s, and $F(t)$ is plotted as shown in Fig. 3.

The transient response of the shell panel is solved by the Newmark-β direct integration method [60], and the parameters α_N and β_N are taken to be 0.5 and 0.25, respectively. All the calculations for transient response were performed using a time step of 0.0005 s, and the initial modal damping ratio was assumed to be 0.8% [38]. The effects of the velocity feedback gain, CNT volume fraction, and CNT distribution type on the transient response of the centre point A ($a/2$, $a/2$) of the hybrid panel were investigated.

First, the active vibration control effect of the velocity feedback controller for the PFG-CNTRC spherical panel was studied. The transient responses of the panel with and without the velocity feedback gain are displayed in Figs. 4, 5 and 6. The Figures show that, in the case of a velocity feedback gain of zero, the transient responses of the panel decrease with time because of structural damping. These Figures also indicate that increasing the velocity feedback gain causes the active damping to become stronger, resulting in a smaller amplitude of the centre point deflection and faster suspension vibration of the hybrid panel. Moreover, the panel is in the free vibration state after the load is removed.

Next, the effects of the volume fraction of CNTs and the distribution type of CNTs on the transient response of the PFG-CNTRC spherical panel were investigated. The effect of the CNT volume fraction is indicated for the uniform distribution (UD) of CNTs with velocity feedback control gain $G_v = 5e{-}5$. The effect of the CNT distribution type is indicated for the CNT volume fraction $V^*_{CNT} = 28\%$ with velocity feedback control gain $G_v = 1.3e{-}5$. Figures 7, 8, and 9 depict the transient responses of the panel associated with stepping load, triangular load, and explosive blast load, respectively. These Figures illustrate that, in all the study cases, the vibration is suppressed faster with an increase in the volume fraction of CNTs. This is compatible with the previous conclusion that addition of CNTs leads to more stiffness of the panels and results in a smaller deflection amplitude. In addition, among the five possible graded patterns of CNTs, FG-O has the largest central deflection, while FG-X has the smallest one. Therefore, the above numerical results demonstrate that, by the proper use of the velocity feedback gain, the vibration of the PFG-CNTRC spherical panels can be controlled as expected.

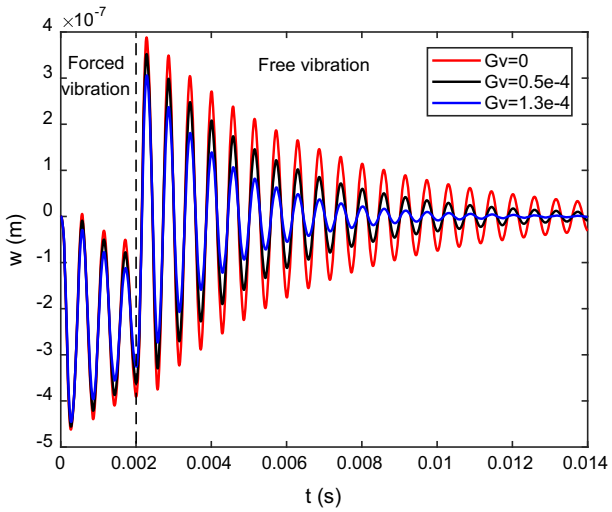

Fig. 4 Central deflection of the PFG-CNTRC spherical panel subjected to step load (UD, $V^*_{\mathrm{CNT}} = 12\%$, CCCC)

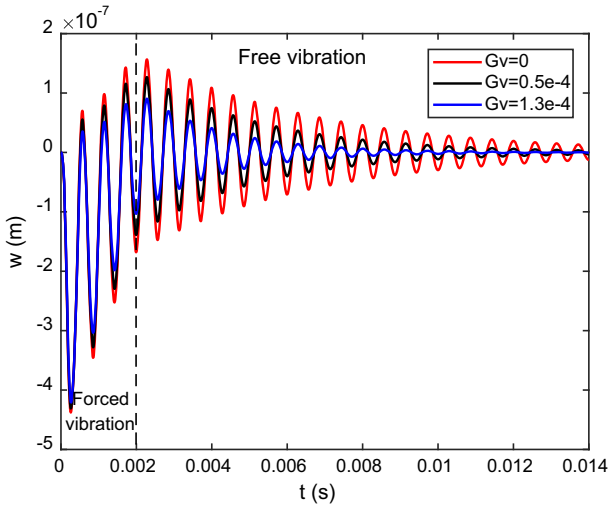

Fig. 5 Central deflection of the PFG-CNTRC spherical panel subjected to triangular load (UD, $V^*_{\mathrm{CNT}} = 12\%$, CCCC)

4 Conclusions

In this study, an efficient finite-element model based on the four-variable shear deformation refined theory was developed for the free vibration and active vibration control of a laminated functionally graded nanotube-reinforced composite with an integrated piezoelectric actuator and sensor layers. The free vibration results were in good agreement with those reported in the literature. Numerical results were provided to explore the effects of the CNT volume fraction, type of CNT distribution, thickness of the piezoelectric layer, laminate configurations, and mechanical and electrical boundary conditions on the natural frequencies of the hybrid spherical panel. A closed-loop control algorithm based on the displacement and velocity feedback was used for active vibration control of the piezoelectric FG-CNTRC spherical panel. As a result of the present formulation and numerical results, some conclusions can be drawn. (i) The volume fraction of CNTs has strong effects on the dynamic responses of the PFG-CNTRC panels. (ii) The natural frequencies of the PFG-CNTRC panel with an open-circuit electrical boundary condition are always higher than those in the closed-circuit case for the same other inlet parameters. (iii) Active vibration control is more effective for the panels with higher stiffness. (iv) The vibration of the PFG-CNTRC spherical panels can be controlled as expected by the proper use of the velocity feedback gain.

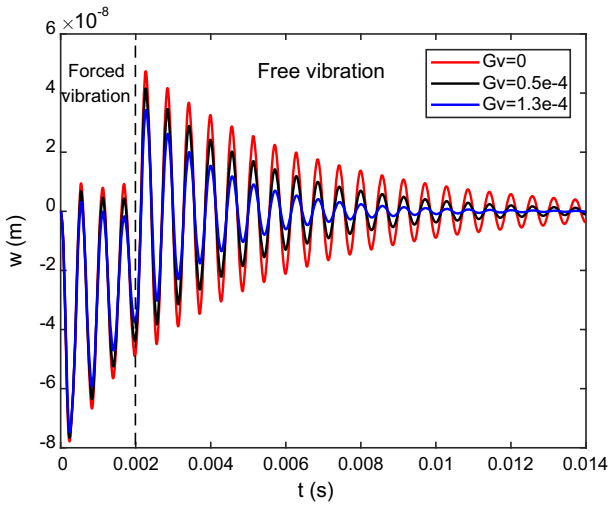

Fig. 6 Central deflection of the PFG-CNTRC spherical panel subjected to explosive blast load (UD, $V^*_{\mathrm{CNT}} = 12\%$, CCCC)

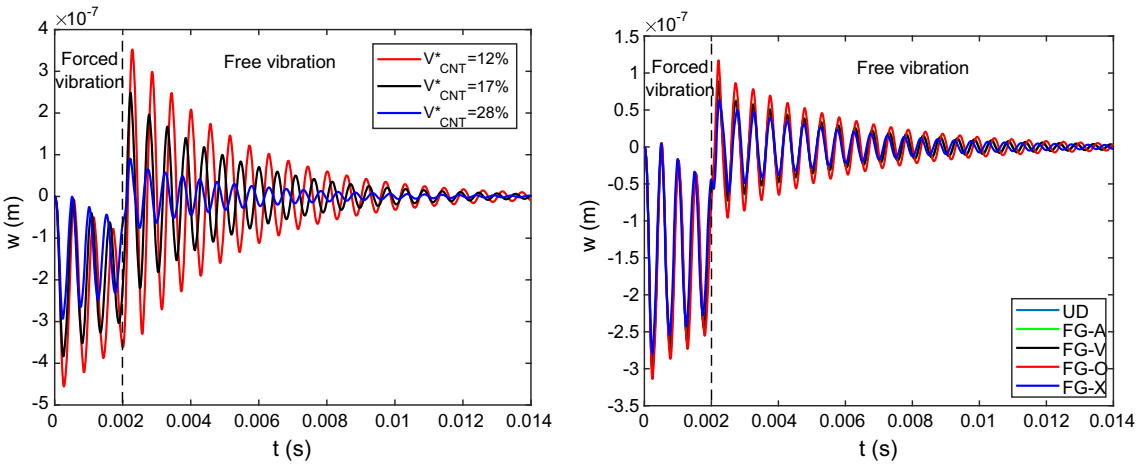

(a) $G_v = 5e{-}5$, FG-UD **(b)** $G_v = 1.3e{-}5$, $V^*_{CNT} = 28\%$

Fig. 7 Transient response of the PFG-CNTRC spherical panel subjected to step load

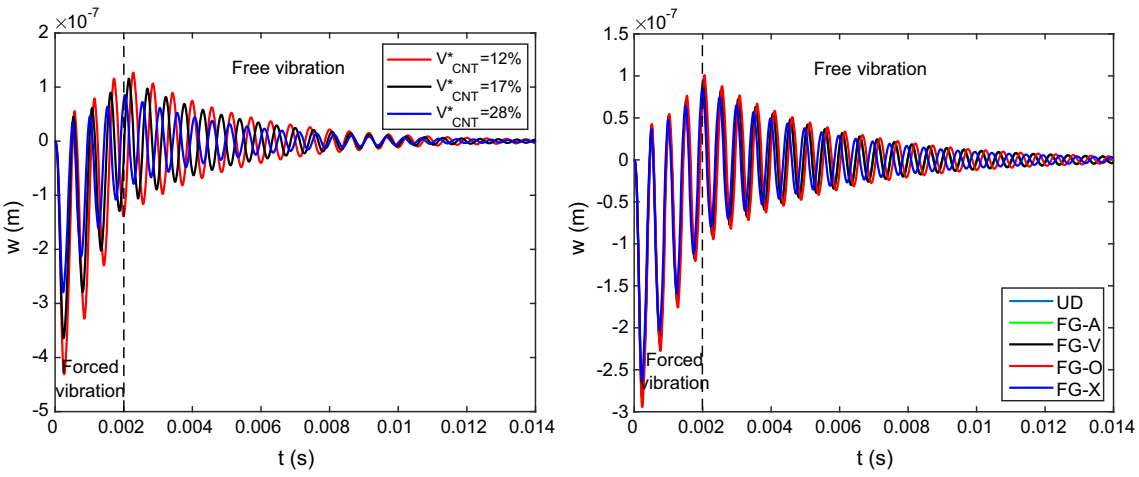

(a) $G_v = 5e{-}5$, FG-UD **(b)** $G_v = 1.3e{-}5$, $V^*_{CNT} = 28\%$

Fig. 8 Transient response of the PFG-CNTRC spherical panel subjected to triangular load

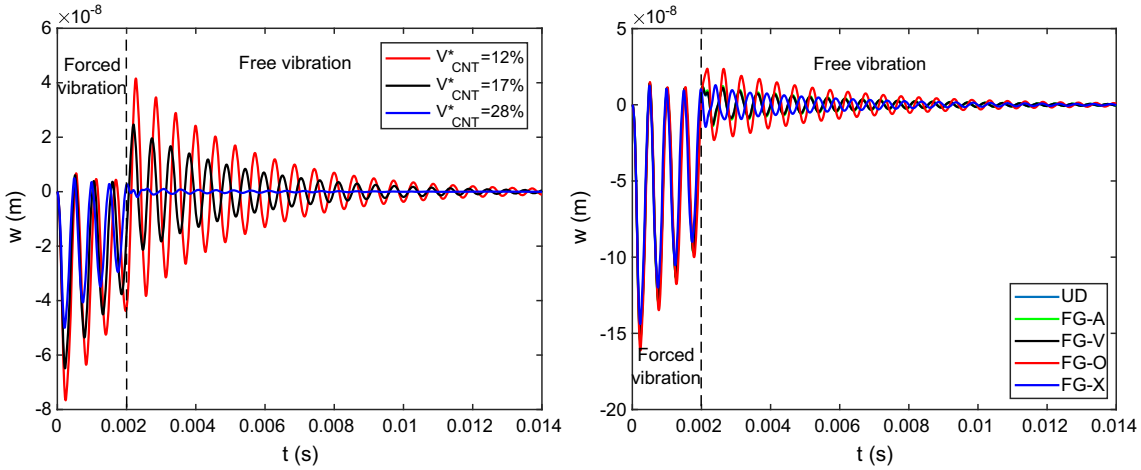

(a) $G_v = 5e{-}5$, FG-UD **(b)** $G_v = 1.3e{-}5$, $V^*_{CNT} = 28\%$

Fig. 9 Transient response of the PFG-CNTRC spherical panel subjected to explosive blast load

Acknowledgments This work was supported by the Foundation for Science and Technology Development of the National University of Civil Engineering, Ha Noi, Vietnam (Project Code 26-2020/KHXD-TĐ).

Compliance with ethical standards

Conflict of interests The authors declare no conflict of interest in preparing this article.

References

1. Ansari, R., Gholami, R., Ajori, S.: Torsional vibration analysis of carbon nanotubes based on the strain gradient theory and molecular dynamic simulations. J. Vib. Acoust. **135**(5), 051016 (2013)
2. Khademolhosseini, F., Phani, A.S., Nojeh, A., Rajapakse, N.: Nonlocal continuum modeling and molecular dynamics simulation of torsional vibration of carbon nanotubes. IEEE Trans. Nanotechnol. **11**(1), 34–43 (2011)
3. Zenkour, A.M.: Torsional dynamic response of a carbon nanotube embedded in visco-Pasternak's medium. Math. Model. Anal. **21**(6), 852–868 (2016)
4. Zenkour, A.: Nonlocal elasticity and shear deformation effects on thermal buckling of a CNT embedded in a viscoelastic medium. Eur. Phys. J. Plus **133**(5), 196 (2018)
5. Zhang, L., Song, Z., Liew, K.: Nonlinear bending analysis of FG-CNT reinforced composite thick plates resting on Pasternak foundations using the element-free IMLS-Ritz method. Compos. Struct. **128**, 165–175 (2015)
6. Zhang, L., Liew, K.: Large deflection analysis of FG-CNT reinforced composite skew plates resting on Pasternak foundations using an element-free approach. Compos. Struct. **132**, 974–983 (2015)
7. Zhang, L., Liew, K.: Geometrically nonlinear large deformation analysis of functionally graded carbon nanotube reinforced composite straight-sided quadrilateral plates. Comput. Methods Appl. Mech. Eng. **295**, 219–239 (2015)
8. Zhang, L., Liu, W., Liew, K.: Geometrically nonlinear large deformation analysis of triangular CNT-reinforced composite plates. Int. J. Non-Linear Mech. **86**, 122–132 (2016)
9. Zhang, L., Song, Z., Liew, K.: State-space Levy method for vibration analysis of FG-CNT composite plates subjected to in-plane loads based on higher-order shear deformation theory. Compos. Struct. **134**, 989–1003 (2015)
10. Zhang, L., Zhang, Y., Zou, G., Liew, K.: Free vibration analysis of triangular CNT-reinforced composite plates subjected to in-plane stresses using FSDT element-free method. Compos. Struct. **149**, 247–260 (2016)
11. Zhang, L., Xiao, L., Zou, G., Liew, K.: Elastodynamic analysis of quadrilateral CNT-reinforced functionally graded composite plates using FSDT element-free method. Compos. Struct. **148**, 144–154 (2016)
12. Zhang, L.: On the study of the effect of in-plane forces on the frequency parameters of CNT-reinforced composite skew plates. Compos. Struct. **160**, 824–837 (2017)
13. Zhang, L., Cui, W., Liew, K.: Vibration analysis of functionally graded carbon nanotube reinforced composite thick plates with elastically restrained edges. Int. J. Mech. Sci. **103**, 9–21 (2015)
14. Lei, Z., Zhang, L., Liew, K.: Elastodynamic analysis of carbon nanotube-reinforced functionally graded plates. Int. J. Mech. Sci. **99**, 208–217 (2015)
15. Zhang, L., Song, Z., Qiao, P., Liew, K.: Modeling of dynamic responses of CNT-reinforced composite cylindrical shells under impact loads. Comput. Methods Appl. Mech. Eng. **313**, 889–903 (2017)

16. Lei, Z., Zhang, L., Liew, K.: Analysis of laminated CNT reinforced functionally graded plates using the element-free kp-Ritz method. Compos. B Eng. **84**, 211–221 (2016)
17. Lei, Z., Zhang, L., Liew, K.: Free vibration analysis of laminated FG-CNT reinforced composite rectangular plates using the kp-Ritz method. Compos. Struct. **127**, 245–259 (2015)
18. Bouazza, M., Zenkour, A.M.: Vibration of carbon nanotube-reinforced plates via refined nth-higher-order theory. Arch. Appl. Mech. **90**, 1755–1769 (2020)
19. Liew, K.M., Pan, Z., Zhang, L.-W.: The recent progress of functionally graded CNT reinforced composites and structures. Sci. China Phys. Mech. Astron. **63**(3), 234601 (2020)
20. Sobhy, M., Zenkour, A.M.: Magnetic field effect on thermomechanical buckling and vibration of viscoelastic sandwich nanobeams with CNT reinforced face sheets on a viscoelastic substrate. Compos. B Eng. **154**, 492–506 (2018)
21. Zenkour, A.M., El-Shahrany, H.D.: Control of a laminated composite plate resting on Pasternak's foundations using magnetostrictive layers. Arch. Appl. Mech. **90**, 1943–1959 (2020)
22. Zenkour, A., El-Shahrany, H.: Vibration suppression analysis for laminated composite beams embedded actuating magnetostrictive layers. J. Comput. Appl. Mech. **50**(1), 69–75 (2019)
23. Zenkour, A.M., El-Shahrany, H.D.: Vibration suppression of advanced plates embedded magnetostrictive layers via various theories. J. Mater. Res. Technol. **9**, 4727–4748 (2020)
24. Zenkour, A., El-Shahrany, H.: Vibration suppression of magnetostrictive laminated beams resting on viscoelastic foundation. Appl. Math. Mech. **41**(8), 1269–1286 (2020)
25. Alibeigloo, A.: Static analysis of functionally graded carbon nanotube-reinforced composite plate embedded in piezoelectric layers by using theory of elasticity. Compos. Struct. **95**, 612–622 (2013)
26. Alibeigloo, A.: Elasticity solution of functionally graded carbon-nanotube-reinforced composite cylindrical panel with piezoelectric sensor and actuator layers. Smart Mater. Struct. **22**(7), 075013 (2013)
27. Alibeigloo, A.: Three-dimensional thermoelasticity solution of functionally graded carbon nanotube reinforced composite plate embedded in piezoelectric sensor and actuator layers. Compos. Struct. **118**, 482–495 (2014)
28. Alibeigloo, A.: Thermoelastic analysis of functionally graded carbon nanotube reinforced composite cylindrical panel embedded in piezoelectric sensor and actuator layers. Compos. B Eng. **98**, 225–243 (2016)
29. Alibeigloo, A.: Free vibration analysis of functionally graded carbon nanotube-reinforced composite cylindrical panel embedded in piezoelectric layers by using theory of elasticity. Eur. J. Mech. A/Solids **44**, 104–115 (2014)
30. Rafiee, M., He, X., Liew, K.: Non-linear dynamic stability of piezoelectric functionally graded carbon nanotube-reinforced composite plates with initial geometric imperfection. Int. J. Non-Linear Mech. **59**, 37–51 (2014)
31. Rafiee, M., Liu, X., He, X., Kitipornchai, S.: Geometrically nonlinear free vibration of shear deformable piezoelectric carbon nanotube/fiber/polymer multiscale laminated composite plates. J. Sound Vib. **333**(14), 3236–3251 (2014)
32. Wu, C.-P., Chang, S.-K.: Stability of carbon nanotube-reinforced composite plates with surface-bonded piezoelectric layers and under bi-axial compression. Compos. Struct. **111**, 587–601 (2014)
33. Nasihatgozar, M., Daghigh, V., Eskandari, M., Nikbin, K., Simoneau, A.: Buckling analysis of piezoelectric cylindrical composite panels reinforced with carbon nanotubes. Int. J. Mech. Sci. **107**, 69–79 (2016)
34. Ansari, R., Pourashraf, T., Gholami, R., Shahabodini, A.: Analytical solution for nonlinear postbuckling of functionally graded carbon nanotube-reinforced composite shells with piezoelectric layers. Compos. B Eng. **90**, 267–277 (2016)
35. Kiani, Y.: Free vibration of functionally graded carbon nanotube reinforced composite plates integrated with piezoelectric layers. Comput. Math. Appl. **72**(9), 2433–2449 (2016)
36. Kolahchi, R., Zarei, M.S., Hajmohammad, M.H., Nouri, A.: Wave propagation of embedded viscoelastic FG-CNT-reinforced sandwich plates integrated with sensor and actuator based on refined zigzag theory. Int. J. Mech. Sci. **130**, 534–545 (2017)
37. Setoodeh, A., Shojaee, M., Malekzadeh, P.: Application of transformed differential quadrature to free vibration analysis of FG-CNTRC quadrilateral spherical panel with piezoelectric layers. Comput. Methods Appl. Mech. Eng. **335**, 510–537 (2018)
38. Nguyen-Quang, K., Vo-Duy, T., Dang-Trung, H., Nguyen-Thoi, T.: An isogeometric approach for dynamic response of laminated FG-CNT reinforced composite plates integrated with piezoelectric layers. Comput. Methods Appl. Mech. Eng. **332**, 25–46 (2018)
39. Selim, B., Yin, B., Liew, K.: Impact analysis of CNT-reinforced composite plates integrated with piezoelectric layers based on Reddy's higher-order shear deformation theory. Compos. B Eng. **136**, 10–19 (2018)
40. Zhang, L., Song, Z., Liew, K.: Optimal shape control of CNT reinforced functionally graded composite plates using piezoelectric patches. Compos. B Eng. **85**, 140–149 (2016)
41. Tran, H.Q., Van, T., Tran, M.T., Nguyen-Tri, P.: A new four-variable refined plate theory for static analysis of smart laminated functionally graded carbon nanotube reinforced composite plates. Mech. Mater. **142**, 103294 (2020)
42. Huu Quoc, T., Minh Tu, T., Van Tham, V.: Free vibration analysis of smart laminated functionally graded CNT reinforced composite plates via new four-variable refined plate theory. Materials **12**(22), 3675 (2019)
43. Song, Z., Zhang, L., Liew, K.: Active vibration control of CNT reinforced functionally graded plates based on a higher-order shear deformation theory. Int. J. Mech. Sci. **105**, 90–101 (2016)
44. Song, Z., Zhang, L., Liew, K.: Active vibration control of CNT-reinforced composite cylindrical shells via piezoelectric patches. Compos. Struct. **158**, 92–100 (2016)
45. Sharma, A., Kumar, A., Susheel, C., Kumar, R.: Smart damping of functionally graded nanotube reinforced composite rectangular plates. Compos. Struct. **155**, 29–44 (2016)
46. Zhang, L., Lei, Z., Liew, K., Yu, J.: Static and dynamic of carbon nanotube reinforced functionally graded cylindrical panels. Compos. Struct. **111**, 205–212 (2014)
47. Selim, B., Zhang, L., Liew, K.: Active vibration control of CNT-reinforced composite plates with piezoelectric layers based on Reddy's higher-order shear deformation theory. Compos. Struct. **163**, 350–364 (2017)
48. Fidelus, J., Wiesel, E., Gojny, F., Schulte, K., Wagner, H.: Thermo-mechanical properties of randomly oriented carbon/epoxy nanocomposites. Compos. A Appl. Sci. Manuf. **36**(11), 1555–1561 (2005)

49. Van Tham, V., Huu Quoc, T., Minh Tu., T. : Free vibration analysis of laminated functionally graded carbon nanotube-reinforced composite doubly curved shallow shell panels using a new four-variable refined theory. J. Compos. Sci. **3**(4), 104 (2019)
50. Shen, H.-S.: Nonlinear bending of functionally graded carbon nanotube-reinforced composite plates in thermal environments. Compos. Struct. **91**(1), 9–19 (2009)
51. El Meiche, N., Tounsi, A., Ziane, N., Mechab, I.: A new hyperbolic shear deformation theory for buckling and vibration of functionally graded sandwich plate. Int. J. Mech. Sci. **53**(4), 237–247 (2011)
52. Ray, M., Sachade, H.: Finite element analysis of smart functionally graded plates. Int. J. Solids Struct. **43**(18–19), 5468–5484 (2006)
53. Zenkour, A.M., Alghanmi, R.A.: Bending of exponentially graded plates integrated with piezoelectric fiber-reinforced composite actuators resting on elastic foundations. Eur. J. Mech. A/Solids **75**, 461–471 (2019)
54. Shiyekar, S., Kant, T.: Higher order shear deformation effects on analysis of laminates with piezoelectric fibre reinforced composite actuators. Compos. Struct. **93**(12), 3252–3261 (2011)
55. Reddy, J.N.: Mechanics of Laminated Composite Plates and Shells: Theory and Analysis. CRC Press, Boca Raton (2004)
56. Farsangi, M.A., Saidi, A.: Levy type solution for free vibration analysis of functionally graded rectangular plates with piezoelectric layers. Smart Mater. Struct. **21**(9), 094017 (2012)
57. Farsangi, M.A., Saidi, A., Batra, R.: Analytical solution for free vibrations of moderately thick hybrid piezoelectric laminated plates. J. Sound Vib. **332**(22), 5981–5998 (2013)
58. Rouzegar, J., Abad, F.: Free vibration analysis of FG plate with piezoelectric layers using four-variable refined plate theory. Thin Walled Struct. **89**, 76–83 (2015)
59. Sayyaadi, H., Farsangi, M.A.A.: An analytical solution for dynamic behavior of thick doubly curved functionally graded smart panels. Compos. Struct. **107**, 88–102 (2014)
60. Newmark, N.M.: A method of computation for structural dynamics. J. Eng. Mech. Div. **85**(3), 67–94 (1959)